THE ASTROPHYSICAL JOURNAL, 598:610–625, 2003 November 20

BURIED ALIVE IN THE CORONAL GRAVEYARD

THOMAS R. AYRES, ALEXANDER BROWN, AND GRAHAM M. HARPER
Center for Astrophysics and Space Astronomy, 389 UCB, University of Colorado, Boulder, CO 80309-0389;
ayres@casa.colorado.edu, ab@casa.colorado.edu, gmh@casa.colorado.edu
Received 2002 December 19; accepted 2003 July 22

ABSTRACT

We have used the High Resolution Camera (HRC-I) of the *Chandra X-Ray Observatory* to search for coronal ($T \sim 10^6$ K) emission from the archetype "noncoronal" red giants Arcturus (α Bootis=HD 124897, K1 III) and Aldebaran (α Tauri=HD 29139, K5 III). Our program follows up previous detections of ultraviolet coronal proxies such as C IV λ1548 ($T \sim 1 \times 10^5$ K) and O VI λ1031 ($T \sim 3 \times 10^5$ K). The deep ($\sim$19 ks) HRC-I pointings obtained a tentative 3 σ detection of Arcturus, with $f_X(0.2\text{–}2\ \mathrm{keV}) = 1.0^{+1.8}_{-0.8} \times 10^{-15}$ ergs cm^{-2} s^{-1} (95% confidence limits [CLs]), but failed to record Aldebaran, with an upper limit of $\lesssim 1.5 \times 10^{-15}$ ergs cm^{-2} s^{-1} (also at 95% CL). The corresponding L_X/L_{bol} ratios are a factor of *ten thousand* less than the Sun, a low-activity coronal dwarf. At the same time, *Hubble* Space Telescope Imaging Spectrograph far-ultraviolet spectra suggest the presence of a "cool absorber," probably near the base of the red giant chromosphere, imprinting discrete low-excitation absorptions on top of highly ionized features such as Si IV λ1393. The hot emission zones thus are at least partially buried under a large column of chromospheric material, which would severely attenuate any soft X-rays that might be emitted. The submerged hot structures presumably are magnetic because of their high temperatures and broad C IV profiles (FWHM $\sim$ 130 km s^{-1}). Perhaps these structures are analogous to small-scale ephemeral bipolar regions seen ubiquitously on the Sun throughout the sunspot cycle and thought to be of direct convective origin. If small-scale magnetic fields indeed are present in the lower atmospheres of red giants such as Arcturus and Aldebaran, they might play a role in initiating the cool winds of such stars, perhaps through a mechanism similar to solar spicules.

Subject headings: stars: coronae — stars: individual (Aldebaran, Arcturus) — ultraviolet: stars — X-rays: stars

1. INTRODUCTION

Low-mass stars begin their lives as fast-spinning dwarfs that emit copious coronal ($T \sim 10^6$ K) X-rays because of intense rotation-catalyzed dynamo-driven magnetic activity (see, e.g., Tuominen, Moss, & Rüdiger 1991; Parker 1970). Such stars end their lives as bloated red giants that rotate slowly if at all (Gray & Pallavicini 1989), thanks to persistent angular momentum loss by the magnetized coronal wind during the long main-sequence phase. These old spun-down stars are expected to display only feeble magnetic activity at best. Indeed, single red giants across the "Linsky-Haisch dividing line" near K1 III rarely were detected in early surveys of coronal proxy C IV ($T \sim 10^5$ K) with the *International Ultraviolet Explorer* (Linsky & Haisch 1979), in X-rays initially with the *Einstein* Observatory (Ayres et al. 1981a), or later in very deep *ROSAT* pointings (e.g., Ayres, Fleming, & Schmitt 1991). Accordingly, the empty region of the X-ray H-R diagram across the Linsky-Haisch dividing line has come to be called the "coronal graveyard."

There are other reasons—beyond the simple suppression of dynamo action by slow rotation—that explain the absence of X-ray sources in the coronal graveyard: (1) simulations of magnetic flux rope evolution in giant stars suggest that such structures will be trapped near the radiative core and not be buoyantly transported to the stellar surface (Holzwarth & Schüssler 2001); (2) even if magnetic loops manage to rise to the surface, the low gravities of the evolved stars are thought to enforce a thermal instability that would prevent loop temperatures from exceeding a few times 10^4 K (Antiochos, Haisch, & Stern 1986); and (3) even if hot loops were possible on the old red giants, the Linsky-Haisch boundary coincides with the development of strong cool winds in such stars, suggesting that the energy that otherwise would heat the coronal loops somehow is being diverted to power the mass flux instead (Linsky & Haisch 1979).

Observations by the *Hubble Space Telescope* (*HST*) ultraviolet spectrographs Goddard High Resolution Spectograph (GHRS) and Space Telescope Imaging Spectrograph (STIS) have shown, however, that the earlier reports of the death of red giant coronae were premature and that magnetic activity might still be lingering on such stars. For example, the noncoronal giant γ Dra (K5 III) was not only detected at C IV in an early GHRS observation but also recorded as a faint X-ray source in a 19 ks pointing with the *ROSAT* Position Sensitive Proportional Counter (PSPC; Brown, Linsky, & Ayres 1993). Subsequent deep far-UV spectroscopy with GHRS by Ayres et al. (1997) clearly detected the coronal proxy Si IV ($T \sim 6 \times 10^4$ K) in other noncoronal red giants, at L(Si IV)/L_{bol} levels only a few times lower than typical low-activity—but coronal—K0 giants such as Pollux (β Gem, K0 III).

Inspired by these positive results we revisited the question of coronal activity on the noncoronal giants, using the sensitive "solar-blind" High Resolution Camera (HRC-I) of the *Chandra X-Ray Observatory* to search for 0.2–10 keV emission from the two optically brightest K giants: Arcturus (α Boo, K1 III) and Aldebaran (α Tau, K5 III), both well-established members of the noncoronal class. As part of the *Chandra* program, *HST* STIS recorded the 1150–1710 Å

region of Aldebaran at medium echelle resolution ($\lambda/\Delta\lambda \sim 4 \times 10^4$) to compare with existing STIS far-UV spectra of Arcturus. Aldebaran had been observed previously with GHRS but only in a few isolated spectral windows (Robinson, Carpenter, & Brown 1998). Here we describe the new HRC-I pointings, supporting ultraviolet spectra from *HST* and the *Far-Ultraviolet Spectroscopic Explorer* (*FUSE*), and the insights we have gained concerning the presence of hot emission regions on these old cold stars.

2. OBSERVATIONS

2.1. *Chandra High Resolution Camera*

The *Chandra X-Ray Observatory* has been described by Weisskopf, O'Dell, & van Speybroeck (1996) and the HRC-I by Murray et al. (1997). *Chandra* HRC-I has three important advantages for detecting weak X-ray emission from optically bright stars: (1) subarcsecond imaging and absolute astrometry minimize source confusion; (2) high spatial resolution also suppresses the cosmic background, by resolving the ubiquitous extragalactic point sources and spreading any truly diffuse component over many pixels; and (3) perhaps most importantly, HRC-I can observe visually bright targets that nevertheless are X-ray faint, whereas the CCD cameras of *XMM-Newton* EPIC and *Chandra* ACIS have substantial "red leaks" that make such observations problematic. The HRC-I is sensitive primarily to UV ionizing photons, which generally are lacking in red stars,[1] while the CCDs are most sensitive to optical photons, which the red stars produce in abundance.

The disadvantage of HRC-I is that, while optimized for high spatial resolution, the microchannel plate camera lacks innate energy discrimination and thus is unable to spectrally characterize a source. Our intention, however, was to perform a simple detection experiment: to assess whether sufficient source counts were present to justify a subsequent much deeper exposure with one of the energy-resolving CCD imagers, supposing that the red leak problem could be surmounted.

2.1.1. *HRC-I Observations*

Aldebaran was observed with HRC-I on 2001 December 29 for 18.9 ks, and Arcturus on 2002 June 19 for 18.5 ks, as summarized in Table 1. Several prominent point sources appear in each field, as anticipated from earlier *ROSAT* PSPC pointings, but nothing conspicuous near the center of either image at the predicted target position. We processed the event lists by using custom software (in IDL).

The two HRC-I fields are depicted in Figure 1, superposed on earlier *ROSAT* PSPC pointings. Only the inner portions of the $30' \times 30'$ HRC-I frames are shown because the point-spread function (PSF) degrades rapidly off-axis. The vastly improved resolution of *Chandra* compared with *ROSAT* is apparent, and there is a good correspondence between the detected sources in the overlapping portions of the HRC-I and PSPC images. Most of the sources probably are extragalactic, certainly in the Arcturus field, which is at high Galactic latitude. The one exception is source 3 in the Aldebaran image that is the 11th magnitude Hyades K dwarf BD $+16^\circ 630$ (VB 184). It originally was detected by *Einstein* at a coronal luminosity of $L_X = 8 \times 10^{28}$ ergs s^{-1} (Micela et al. 1988).

While the cited absolute astrometric precision of *Chandra* imaging is excellent ($0\farcs6$ at 90% confidence limits [CLs][2]), it usually is possible to refine the pointing center of an observation by matching the apparent sources with an optical catalog such as the US Naval Observatory A2.0. Unfortunately, this is not practical for our particular observations because the existing catalogs have significant "holes" at the positions of our targets: the original survey plates, on which the digital catalogs are based, are heavily overexposed in the vicinity of very bright stars, preventing the detection of fainter objects nearby. The USNO A2 catalog, for example, becomes significantly populated only at $r \gtrsim 10'$ from Aldebaran and Arcturus, the point where the *Chandra* PSF has degraded sufficiently that accurate astrometry of the X-ray sources is compromised. Fortunately, the normal astrometric pointing precision of *Chandra* is adequate for our purposes here.

2.1.2. *X-Ray Measurements*

To establish reliable X-ray detections in the HRC-I fields, one must choose an appropriate detect cell size. A larger cell potentially collects more source photons but at the expense of increased background counts. A smaller cell minimizes the background but at the expense of requiring a larger correction for the "missed" photons outside the particular encircled energy radius. In general, the optimum detect cell balancing these two considerations corresponds to ~75% encircled energy.

We determined the encircled energy profile of HRC-I by using deep archival pointings on the calibration target AR Lacertae, an X-ray–bright RS CVn binary. We obtained a 75% encircled energy radius of $r \sim 0\farcs7$. (Coincidentally, this also is comparable to the expected astrometric accuracy.) A similar analysis for *ROSAT,* by using AR Lac and the bright BL Lac object Mrk 421, indicated $r \sim 25''$ for the

[1] See http://cxc.harvard.edu/ccw/proceedings/02_proc/presentations/m_zombeck/index.html.

[2] See http://asc.harvard.edu/cal/ASPECT.

TABLE 1
Chandra HRC-I Observations

Name	Sequence	Observation ID	UT Start	t_{exp} (ks)	C_X (counts s^{-1})
α Tau	200162	2554	2001 Dec 29.08	18.87	$\lesssim 2.3 \times 10^{-4}$
α Boo	200163	2555	2002 Jun 19.02	18.48	$1.5^{+2.7}_{-1.2} \times 10^{-4}$

Note.—Count rates C_X are for the 75% encircled energy detect cell, at 95% CL.

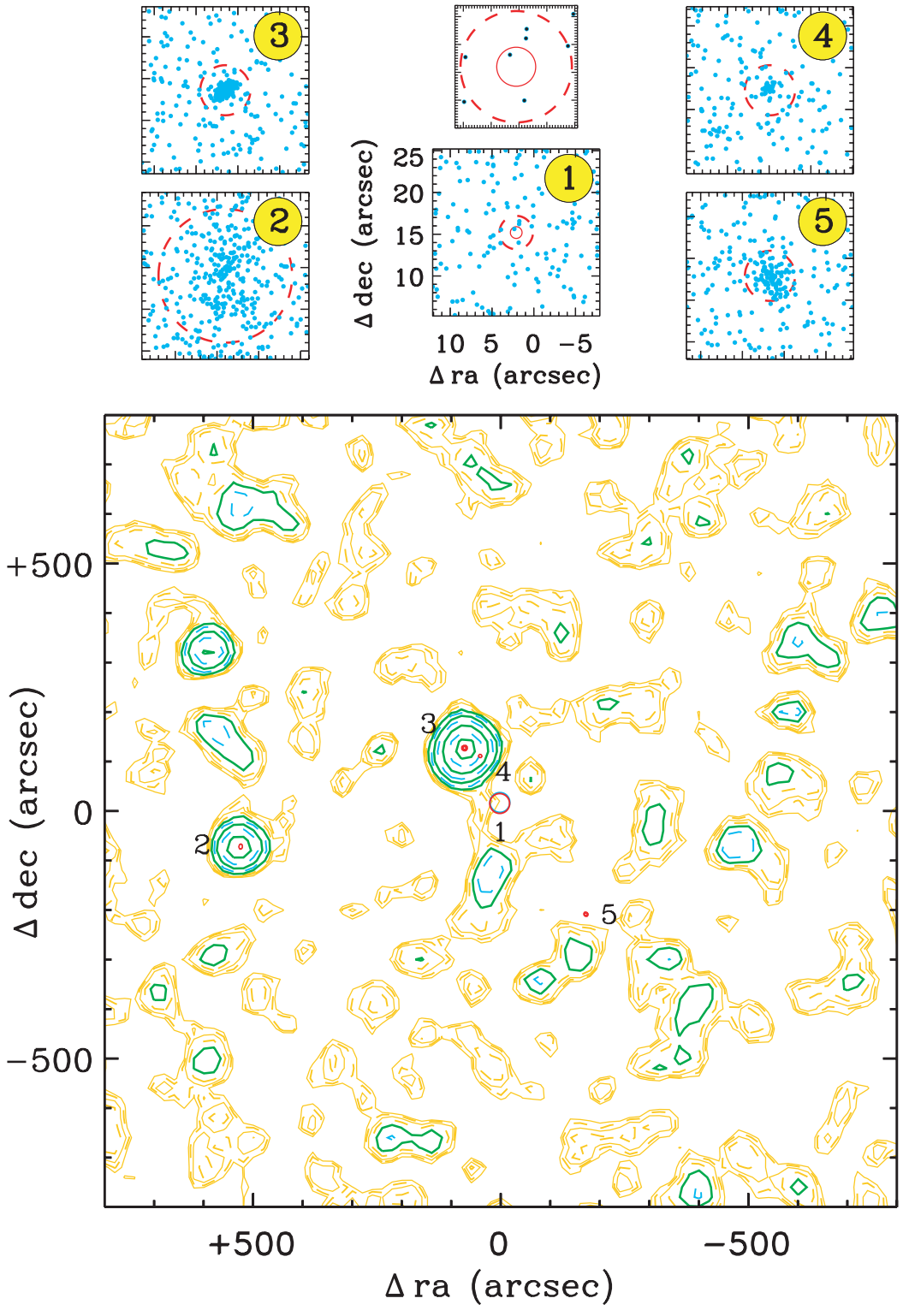

FIG. 1*a*

FIG. 1.—(*a*) HRC-I observation of Aldebaran compared with *ROSAT* PSPC image from a decade earlier. The ordinate and abscissa are relative sky coordinates with respect to the pointing center of the observation. The PSPC frame is depicted as logarithmic contours relative to the peak count rate: multiple green contours indicate significant X-ray enhancements over background; lighter yellow contours indicate smaller enhancements. The HRC-I field is represented by the (compact) red contours. The 25 times higher spatial resolution of the HRC-I is evident. The four brightest HRC-I sources are labeled 2–5 and are shown as individual X-ray events in the upper panels. Position 1 is the expected location of the target. A blue circle indicates the predicted position in the PSPC era; a red circle marks the position in the more recent *Chandra* epoch (the two nearly coincide for Aldebaran because of its small proper motion). Source 3 is the Hyades star VB 184. Weaker source 4 is not apparent in the PSPC map but is fully separated from 3 at HRC-I resolution. In the upper panels, the smallest dashed reference circle is 2″ in radius, medium circles are 3″, and the largest circle is $r = 8''$. The small solid circle is 0.″7 in radius, corresponding to the 75% encircled energy detect cell for HRC-I. Above panel 1 is an expanded view of the inner ±2″ centered on the predicted source position. (*b*) For Arcturus. The significant displacement of the target between the *ROSAT* and *Chandra* epochs is due to its large proper motion. Note the cluster of 3 counts near field center, close to the predicted target position.

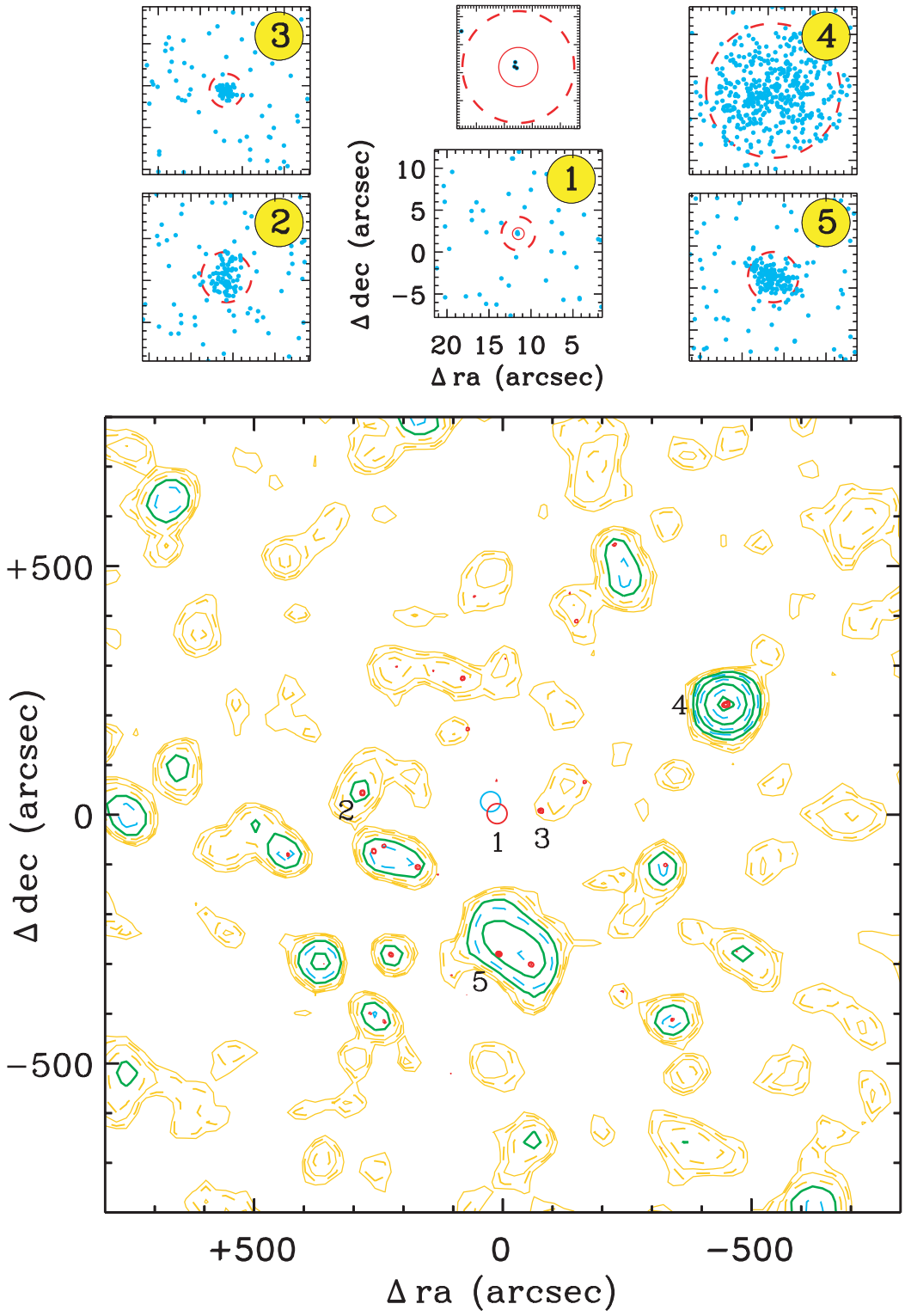

FIG. 1*b*

PSPC (at 75% encircled energy for pulse height channels 24–200). For typical background radiation conditions, the PSPC would accumulate about 10 counts in 20 ks in the $r = 25''$ source circle, while HRC-I would record less than 1 count in its detect cell. Adopting the optimum cells for the different instruments ensures the fairest comparison between the resulting measurements.

In addition to choosing an appropriate detect radius, one also must establish scaling rules to determine the significance of an apparent count excess or to set upper limits, given the measured average background count rate. We employed Monte Carlo simulations of the Poisson counting process and determined that the 3 σ detection threshold (corresponding to 0.13% probability of a false positive

detection in a one-sided Gaussian distribution; see, e.g., Gehrels 1986) is $3\sqrt{B}+1.6$, where B is the average background count in the detect cell. [Note that this result refers to the *significance* of a detection with respect to fluctuations in the background. Gehrels' often-quoted formula, $C_s \sim s(N+1)^{1/2}+(s^2+2)/3$, where $s=3$ for the 3 σ case, refers to the *upper bound of possible source fluxes* at that confidence level given a measured source count of N, assuming a negligible background. If $B \lesssim 1$, one can have a highly significant source detection with only a few counts in the cell, but, according to Gehrels' formula, knowledge of the true source flux will be very imprecise.]

Our measurements of the Aldebaran and Arcturus HRC-I images near the predicted target locations indicated backgrounds of 0.41 counts arcsec^{-2} in 18.9 ks for the former and 0.13 counts arcsec^{-2} in 18.5 ks for the latter. The Aldebaran background is about twice the nominal quiescent rate of 9×10^{-6} counts s^{-1} arcsec^{-2}, while the Arcturus background is lower than the nominal value, probably mostly because of different solar activity conditions.

The Aldebaran image has a single count in the $r \sim 0\farcs7$ detect cell compared with an expected background of 0.6 and thus is considered a nondetection. Using the count limits appropriate to this case from Table 2 of Kraft, Burrows, & Nousek (1991), we obtain an upper limit source count rate of $C_X \lesssim 2.3 \times 10^{-4}$ counts s^{-1} at 95% CL.

The Arcturus image, on the other hand, has a cluster of 3 counts in the detect cell compared with an expected background of 0.2. According to our criterion, above, this represents a highly significant fluctuation at the 3 σ level—very unlikely to occur by pure chance—and thus possibly is a valid detection. Applying the Kraft et al. (1991) count limits appropriate to this case yields $C_X = 1.5^{+2.7}_{-1.2} \times 10^{-4}$ counts s^{-1} at 95% CL, in the 75% encircled energy detect cell. Again, although the source *detection* is at a very high confidence level (>99.8%), the range of possible source fluxes consistent with the detected 3 counts is quite large. We also note that in X-ray astronomy it is common to reserve "significant detections" for those at the 4 σ level or higher (Hasinger et al. 1998). This conservative limit ($1-\mathrm{CL} \sim 3 \times 10^{-5}$ for a one-sided Gaussian distribution) comes about from "blind" identifications in an X-ray field, without regard to an input list of possible source positions, where there is a strong desire to minimize the number of false positive detections (see, e.g., Watson et al. 2001). In a typical case with, say, $n \sim$ a few times 10^4 independent resolution elements in an X-ray image, one must set $1-\mathrm{CL} \lesssim 1/n$ to minimize false positives in that field. However, here we are taking a more Bayesian viewpoint by introducing prior knowledge (of the potential source position) and asking the question of how significant a count excess might be located there.

Simulations with the WebPIMMS count rate tool[3] using solar-abundance Raymond-Smith models at several temperatures between $\log T = 5.8$ and 6.8 K indicated an energy conversion factor (ECF) of $\sim 5 \times 10^{-12}$ ergs cm^{-2} count^{-1} for *Chandra* HRC-I for the reference band 0.2–2 keV, with an uncertainty of about $\pm 50\%$ because of the unknown source temperature. Thus, the 95% CL limit fluxes for Arcturus and Aldebaran are $1.0^{+1.8}_{-0.8} \times 10^{-15}$ and $\lesssim 1.5 \times 10^{-15}$ ergs cm^{-2} s^{-1}, respectively, including compensation for the encircled energy factor.

[3] See http://legacy.gsfc.nasa.gov/Tools/w3pimms.html.

The HRC-I detection thresholds are significantly lower than achieved previously with *ROSAT*. We remeasured the available PSPC event lists for Arcturus (data set rp150018n00: 18.1 ks) and Aldebaran (rp200073n00: 2.3 ks) from the *ROSAT* public archive at HEASARC. Ayres et al. (2003) describe the measurement strategy, although they used a larger nominal encircled energy radius to capture the soft counts used in determining a hardness ratio. Here we adopted the optimum PSPC detect cell and ECF $\sim 1 \times 10^{-11}$ ergs cm^{-2} count^{-1} to convert from channel 24–200 count rate to 0.2–2 keV flux. We found 95% CL upper limits of $f_X \lesssim 6 \times 10^{-15}$ for Arcturus and $\lesssim 1.7 \times 10^{-14}$ ergs cm^{-2} s^{-1} for Aldebaran. The original PSPC upper limit for Arcturus reported by Ayres et al. (1991) is a factor of 3 smaller than the PSPC upper limit obtained here, mostly because of a correspondingly smaller ECF (3×10^{-12} ergs cm^{-2} count^{-1}) used to convert channel 10–240 counts into 0.1–2.4 keV flux, assuming a very soft source. The ECF for our more restricted reference energy band is much less sensitive to the unknown source temperature. Again, the important consideration is that we compare the HRC-I and PSPC pointings on as similar a footing as possible.

The HRC-I 0.2–2 keV X-ray luminosities are $L_X = 1.5^{+2.6}_{-1.2} \times 10^{25}$ ergs s^{-1} at the 11 pc distance of Arcturus and $L_X \lesssim 7 \times 10^{25}$ ergs s^{-1} at the 20 pc distance of Aldebaran. By way of comparison, the average L_X of the Sun in the same energy band is about 2 orders of magnitude larger (Judge, Solomon, & Ayres 2003), despite the fact that the Sun has less than one-hundredth the surface area of a red giant. Because the Sun itself is considered a low-activity object (Schmitt 1997) and given that even minuscule brown dwarfs have already been detected in X-rays by *ROSAT* (e.g., Neuhauser & Comeron 1998; Rutledge et al. 2000), the two red giants must hold the record for coronal futility among all late-type stars.

Figure 2 summarizes these developments in an X-ray/C IV flux-flux diagram, including the new HRC-I measurements for α Boo and α Tau, the PSPC upper limits for those stars, and additional PSPC detections for three comparison red giants: "noncoronal" γ Dra, low-activity Pollux, and high-activity ι Cap (G8 III). The highlighted areas indicate where certain classes of stars tend to congregate, usually displaying power-law correlations between their X-ray and C IV activity indices (Ayres et al. 1995). Although active late G and early K giants for the most part lie on or close to the main-sequence power-law wedge, the noncoronal K giants clearly fall away from an extrapolation of region 4, possibly lying instead at the foot of the X-ray–deficient supergiants locus, or simply displaying a break at $L_X/L_{bol} \sim L(\mathrm{C\ IV})/L_{bol} \sim 10^{-7}$.

To gain insight into possible causes of the depressed coronal luminosities of the noncoronal giants, we turned to spectral observations by *HST* and *FUSE*. Together, these observatories allow access to diagnostics covering the broad temperature range from molecules such as CO and H_2 to highly ionized species such as C IV, N V, and O VI.

2.2. *Hubble Space Telescope: STIS and GHRS*

HST STIS has been described by Woodgate et al. (1998). Observations of Aldebaran were carried out on 2002 January 3 over four *HST* orbits. Arcturus was recorded previously, during early STIS operations in *HST* Cycle 7.

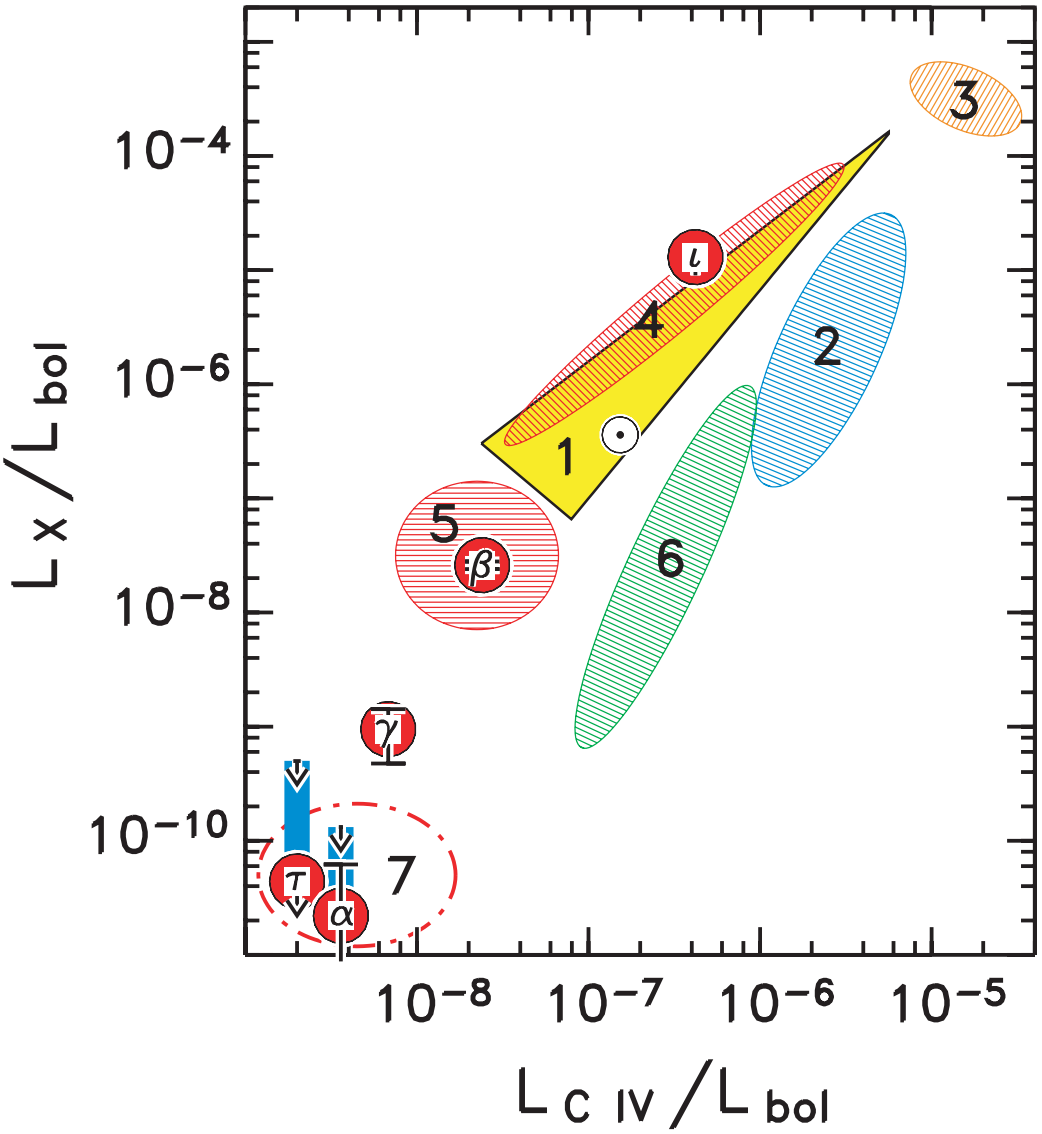

FIG. 2.—X-ray/C IV flux-flux diagram. Normalization by the bolometric fluxes removes the twin biases of different distances and diameters. Shaded zones represent (1) G–K dwarfs (the circled dot marks cycle-average solar ratio), (2) "X-ray–deficient" Hertzsprung gap giants (Simon & Drake 1989), (3) hyperactive RS CVn binaries, (4) active clump (G8–K0) giants, (5) inactive but still coronal K0 giants, (6) G–K supergiants, and (7) noncoronal ($\gtrsim$K1) red giants. Filled red circles mark α Boo ("α"), α Tau ("τ"), and three comparison stars: ι Cap ("ι"), β Gem ("β"), and γ Dra ("γ"). Vertical blue bars connect earlier *ROSAT* upper limits with the new *Chandra* measurements.

Comparison star ι Cap was observed by STIS during Cycle 8. Table 2 summarizes the STIS pointings.

Initial acquisition of Aldebaran was performed by the STIS CCD camera with neutral-density filter F25ND5, followed by a PEAKUP with the CCD+G430M grating and $0\farcs2 \times 0\farcs09$ slit to accurately center the target. Science exposures were taken with the high-throughput $0\farcs2 \times 0\farcs2$ slot, medium-resolution echelle grating E140M, and FUV/MAMA detector, covering the range 1150–1710 Å with $R \equiv \lambda/\Delta\lambda \sim 4 \times 10^4$. The total E140M integration time was 10.5 ks.

The E140M echellograms were processed with the IDL-based CALSTIS package developed by the STIS instrument team at Goddard Space Flight Center (Lindler 1999). It is designed to remove scattered light contributed by bright emission lines, which can affect fainter features in nearby echelle orders. This is particularly important for the red giants because their far-UV spectra are dominated by extremely bright H I λ1215 Lyα and O I λ1305 triplet emission (see, e.g., Ayres, Moos, & Linsky 1981b).

Zero-point corrections to the STIS wavelength scales were based on PtNe lamp exposures taken intermittently during each observation. The first stellar exposure of the sequence has the most precise wavelength scale because the narrow-aperture PEAKUP performed immediately prior to it accurately centered the target. Subsequent exposures could deviate because of slow drifts of the target in the aperture. The first exposure therefore was adopted as a template, and the later spectra were cross-correlated against it to detect any systematic shifts. Each spectrum then was adjusted to the reference wavelength scale and co-added.

Preliminary reconnaissance of the processed STIS spectra indicated that the Si III λ1206 resonance line was absent in the E140M traces of Arcturus and Aldebaran, although

TABLE 2
HST OBSERVATIONS

Data Set	UT Start	t_{exp} (ks)	Instrument	Aperture (arcsec)	λ_{start} (Å)
ι Cap:[a]					
o5bn40010.....	2000 Apr 15.39	1.86	STIS E140M	0.2 × 0.2	1140
o5bn40020.....	2000 Apr 15.44	8.69	STIS E140M	0.2 × 0.2	1140
o5bn40030.....	2000 Apr 15.65	1.10	STIS E140M	0.2 × 0.2	1140
o5bn41020.....	2000 May 04.02	1.90	STIS E230M	0.2 × 0.06	1720
β Gem:[b]					
z2uz0107t.....	1995 Sep 20.02	0.65	GHRS G200M	2.0	1879
z2uz010ft.....	1995 Sep 20.09	1.31	GHRS G160M	2.0	1531
z2uz010ht.....	1995 Sep 20.14	2.07	GHRS G160M	2.0	1383
z2uz010kt.....	1995 Sep 20.21	0.98	GHRS G160M	2.0	1203
z2uz010nt.....	1995 Sep 20.28	0.76	GHRS ECH-A	2.0	1300
α Boo:[c]					
o4y701020.....	1998 Aug 24.78	2.49	STIS E230M	0.2 × 0.06	1720
o4y701030.....	1998 Aug 24.85	5.21	STIS E140M	0.2 × 0.06	1140
γ Dra:[d]					
z0j7010lm.....	1991 Apr 18.87	3.59	GHRS ECH-A	2.0	1301
z2r90108t	1995 Jul 19.52	2.83	GHRS G200M	2.0	1878
z2r9010at	1995 Jul 19.59	2.83	GHRS G160M	2.0	1529
z2r9010bt	1995 Jul 19.70	2.39	GHRS G160M	2.0	1202
z2r9010et.....	1995 Jul 19.76	3.26	GHRS G160M	2.0	1374
α Tau:[e]					
o6je01010	2002 Jan 03.43	1.82	STIS E140M	0.2 × 0.2	1140
o6je01020	2002 Jan 03.48	8.69	STIS E140M	0.2 × 0.2	1140

NOTE.—Stellar parameters are from SIMBAD; for definition of bolometric flux f_{bol} see Ayres et al. (2003): units are 10^{-7} ergs cm^{-2} s^{-1} at Earth. Distances d are in parsecs.
[a] HD 203387, G8 III, $V = +4.30$, $B-V = +0.88$, $f_{bol} = 6.8$, $d = 66$.
[b] HD 62509, K0 III, $V = +1.15$, $B-V = +1.00$, $f_{bol} = 117$, $d = 10$.
[c] HD 124897, K1.5 III, $V = -0.04$, $B-V = +1.23$, $f_{bol} = 453$, $d = 11$.
[d] HD 164058, K5 III, $V = +2.23$, $B-V = +1.52$, $f_{bol} = 84$, $d = 45$.
[e] HD 29139, K5 III, $V = +0.85$, $B-V = +1.54$, $f_{bol} = 343$, $d = 20$.

clearly visible in the GHRS G160M first-order grating observations of γ Dra. The lack of λ1206 in Arcturus, but presence in γ Dra, was surprising because both stars display Si III λ1892 intersystem line emission of comparable strength. (No observations of the 1900 Å region are available for Aldebaran, unfortunately.) However, a careful examination of the original STIS echellogram images of Arcturus and Aldebaran showed faint but definite emission at λ1206, which is 1 echelle order down from the bright red peak of Lyα. The latter "bleeds" across the Si III order in the very deep exposures of the red giants. Apparently, the processing system overcorrects for the background Lyα intensity, thereby suppressing the Si III feature. A companion ~1 Å wide "absorption feature" appears ~10 Å longward of Lyα line center, where the red peak is affecting the next order up in the echelle pattern. We examined E140M echellograms of a number of other late-type giants, but with weaker Lyα emissions, and found no additional cases of the effect. It presumably is most pronounced in very deep exposures of stars with very bright Lyα emissions, such as the two noncoronal giants here.

We developed a custom extraction of the region around Si III, correcting for the Lyα background by fitting a simple function in the cross-dispersion direction to empirically match the shape of the extended wings of the echelle profile. By this method, we found significant Si III emission in both Arcturus and Aldebaran, consistent with that observed in Pollux and γ Dra (see Fig. 3).

Archival *HST* GHRS spectra of comparison stars Pollux and γ Dra are summarized in Table 2. Unfortunately, the restricted free spectral range of GHRS often left important wavelength intervals unobserved. This is much less of a problem with STIS, since a single E140M echelle exposure covers nearly 600 Å. We dearchived the GHRS data sets, making use of the on-the-fly calibration system, and applied the reduction procedures outlined by Ayres et al. (1998).

2.3. *Far-Ultraviolet Spectroscopic Explorer*

FUSE and its in-flight performance have been described by Moos et al. (2000) and Sahnow et al. (2000). *FUSE* pointings were available only for Aldebaran and Pollux, as summarized in Table 3. The data sets were retrieved from the Multimission Archive at Space Telescope (MAST) and recalibrated with CalFUSE V2.1.6[4] by using the default "event burst" and background options. The individual subexposures were screened for orbital day and night: the respective exposure times are listed in Table 3. For the key O VI $\lambda\lambda$1031, 1037 doublet, we considered only the most sensitive channel (LiF1A). The individual (oversampled) spectra were rebinned by a factor of 4, cross-correlated to reduce global spectral drifts between subexposures, and co-added. Comparison of daytime and nighttime traces

[4] The CalFUSE Pipeline Reference Guide Version 1.3 (maintained by V. Dixon, J. Kruk, and E. Murphy; see http://fusegi.pha.jhu.edu.)

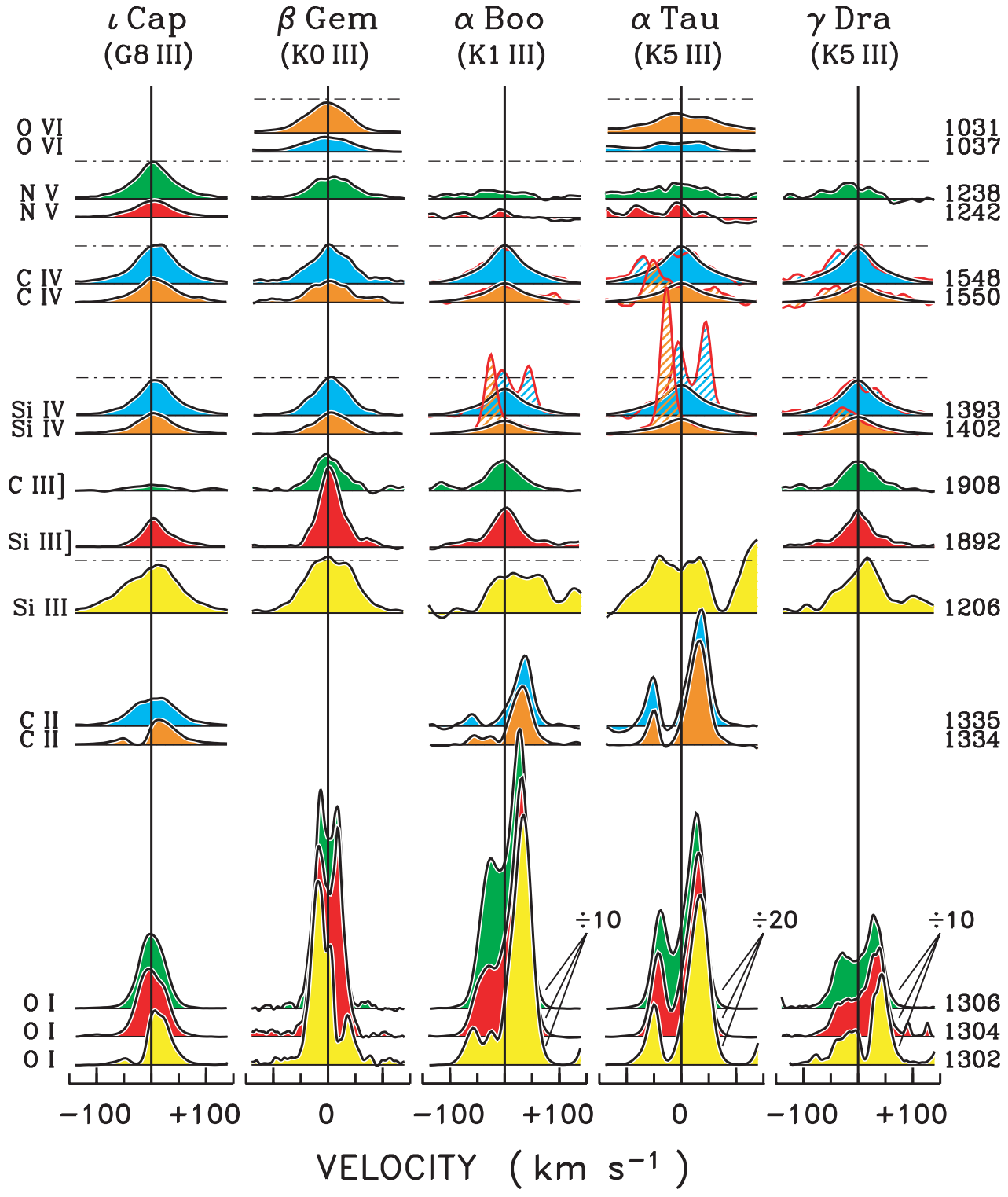

FIG. 3.—Selected ultraviolet emission lines of late-type giants. Features longward of 1200 Å are from *HST* (STIS or GHRS); the O VI profiles are from *FUSE*. "Missing" lines are due to incomplete coverage. Species are arrayed from bottom to top in order of increasing formation temperature, ranging from about 10^4 K for O I up to 3×10^5 K for O VI. A "continuum" level was subtracted from each segment on the basis of a broadband filtering of the surrounding spectrum. The features have the proper relative strengths within each column, and the normalization between the stars was set by the apparent peak flux of C IV λ1548. Note that with such a normalization the O I triplet features (near 1305 Å) of the three later K giants must be scaled down by an order of magnitude or more to fit on the diagram. The velocity scale is relative to the mean chromospheric radial velocity established by weak narrow low-excitation emissions, typically indistinguishable from the optical v_{rad} within measurement errors. Low-velocity narrow interstellar absorption components are visible in O I λ1302 of all the stars except α Tau, and in C II λ1334 of ι Cap and α Boo. For the three "noncoronal" giants (≥K1), the solid shaded profiles of the Si IV and C IV doublets were obtained from a multiple-Gaussian modeling procedure, red curves represent the original features, and hatching highlights the blends with fluoresced lines of H_2 (at Si IV) and Fe II (at C IV).

TABLE 3
FUSE Observations

Name	Data Set	Subexposures	UT Start	t_{exp} (Day) (ks)	t_{exp} (Night) (ks)	Aperture (arcsec)
α Tau	p1040901	8	2001 Jan 14.58	[a]	12	4×20
β Gem	p1180601	7	2000 Nov 11.39	14	7	30×30

[a] Only minimal daytime exposure.

provided a check for airglow contamination. Scattered solar radiation is expected to be minimal in the LiF1A channel.

3. ANALYSIS

3.1. *Ultraviolet Spectral Comparisons*

Figure 3 illustrates selected ultraviolet emission lines of Arcturus, Aldebaran, and the three comparison giants. Table 4 lists fluxes of X-rays and representative hot lines for these stars. The O I triplet at 1305 Å is extremely bright in the two archetypal noncoronal giants, displaying the typical red asymmetric wind-scattered line shapes. C II $\lambda\lambda$1334 and 1335 also show prominent blueshifted wind absorption.

The figure demonstrates that the subcoronal lines of the red giants obey a curious pattern; namely, those falling longward of about 1500 Å are easily recognized (e.g., the C IV doublet at 1549 Å and Si III λ1892+C III λ1909 at longer wavelengths; see Ayres 2000) and have similar line shapes despite the wide gulf in L(C IV)/L_{bol} activity levels seen in Fig. 2. Some of the key hot features falling shortward of 1500 Å, however, are weak or absent. For example, N V λ1238, although definitely present in Arcturus and Aldebaran, is fainter than expected, say from the N V/C IV ratios of Pollux. Furthermore, the λ1242 component is not evident at all: the narrow peaks appearing at its wavelength are C I recombination lines. The weakness of N V might be associated with a more rapid decline in the subcoronal emission measure distribution (the amount of material present as a function of temperature) with increasing T compared with that of the low-activity, but still coronal, Pollux. The weakness of N V probably is *not* due, however, to C I continuum absorption (from a low-lying excited level with its edge at 1240 Å), because such absorption usually either is unimportant ($\tau_C \ll 1$) or complete ($\tau_C \gg 1$), with a sharp transition between the two regimes in column density because of the exponential nature of the extinction process. The presence of O VI also argues against an important role for C I continuum absorption because the strong C I ground-state edge at 1100 Å otherwise would obliterate the $\lambda\lambda$1031, 1037 doublet.

Other hot lines appear to be present, but in reality the features are dominated by coincidental blends: for example, the Si IV $\lambda\lambda$1393, 1402 doublets of the main targets are strongly affected by unfortunately located narrow emissions of the H_2 B–X Lyman system, fluoresced by H I λ1215 Lyα (McMurry, Jordan, & Carpenter 1999). In fact, the strong H_2 B0–X5 P3 transition completely dominates the apparent λ1402 features of Arcturus and Aldebaran, although it is less prominent in γ Dra. Removing the H_2 blends in Si IV would allow us to measure the "pristine" profiles of these important hot lines for comparison with low-activity—but nevertheless coronal—objects such as Pollux, both in terms of emission strengths as well as line shapes (which encode globally average dynamical properties of the subcoronal spectrum).

3.1.1. *Deblending* Si IV*: Initial Approach*

We began the deblending process by accurately determining an intrinsic profile of the optically thin H_2 features by scaling and combining B–X line shapes from other clean members of the fluorescent cascades. The procedure is effective thanks to the high internal precision of the STIS wavelength scales, the broad spectral coverage capturing the full

TABLE 4
Hot-Line and X-Ray Fluxes

Star	Si IV (6×10^4 K)	C IV (1×10^5 K)	N V (2×10^5 K)	O VI (3×10^5 K)	X-Rays [(1–10) $\times 10^6$ K] *ROSAT*	X-Rays [(1–10) $\times 10^6$ K] *Chandra*
ι Cap	21	29	23	...	900[a]	...
β Gem	22	26	13[b]	16	30 ± 4	...
α Boo	10[c]	17[c]	4[b]	...	$\lesssim 0.6$	$0.10^{+0.18}_{-0.08}$
γ Dra	5[c]	6[c]	1.8 ± 0.4[b]	...	0.8 ± 0.4	...
α Tau	5[c]	7[c]	3[b]	3.6 ± 0.4[b]	$\lesssim 1.7$	$\lesssim 0.15$

Note.—Fluxes at Earth, not corrected for interstellar reddening, in units of 10^{-14} ergs cm^{-2} s^{-1}. Line fluxes refer to the sum of the doublet components. X-ray fluxes refer to 0.2–2 keV band, derived either from *Chandra* HRC-I observations discussed here or material from the *ROSAT* archive as described by Ayres et al. (2003); limits are 95% CL. Errors are smaller than a unit increment in the least significant digit, unless stated explicitly.

[a] Average between all-sky survey flux and off-axis PSPC pointing: the two fluxes are somewhat discrepant, probably because of source variability.

[b] Values obtained by scaling from the stronger member of the doublet to the sum by the effectively thin ratio (1.5).

[c] Fluxes deduced from H_2 deblending and multiple-Gaussian modeling (see text).

range of the progressions, and the accurately known molecular wavelengths (Abgrall et al. 1993).

Ideally, next we would simply take the observed fluxes of other lines in the fluorescence progressions, use the known branching ratios to predict the strengths of the three main transitions that corrupt the Si IV doublet, and subtract the properly flux-scaled intrinsic H_2 profiles. We found, however, a number of inconsistencies in the relative strengths of B–X lines in the main progressions. In some cases, several of the potentially available H_2 features were blended with each other or unrelated species. In at least one case (B0–X6 R0, 1454 Å) an expected strong emission was completely absent. Here we take a brief aside to discuss the missing H_2 line because our explanation of its absence will play an important role later. We return to the deblending of the Si IV lines in § 3.1.3.

3.1.2. *Missing* H_2 *Line*

Although a CO transition (A3–X0 P26) falls at the wavelength of the missing H_2 B0–X6 R0 line, the identification is inconsistent with the general absence of other recognizable absorption features from CO lines of similar excitation and oscillator strength. Instead, the absorption likely is from Ni II λ1454.842, arising from the ground state ($E_l = 0$ cm^{-1}). The excited state of Ni II λ1454 branches preferentially to lines in the $\lambda > 2000$ Å region. A search for these features in Arcturus (in an archival high signal-to-noise ratio E230H spectrum) was negative, but the elevated continuum levels at those wavelengths would mask the predicted decay lines in any event. All the other ground-state Ni II lines in the 1200–1700 Å region appear in absorption, including—importantly—λ1393.324, which clips the blue wing of Si IV λ1393.

Figure 4 compares examples of prominent ground-state absorption lines of several different species (taken from the Kurucz line lists: Kurucz & Bell 1995) in the Arcturus and Aldebaran far-UV spectra and in a mean spectrum derived from a group of active giants (see Ayres et al. 2003). The average interstellar features (e.g., in O I λ1302 and Si II λ1260) in the active giant composite are narrow and shifted slightly to the blue (the several giants composing the average were intentionally chosen to have their interstellar medium [ISM] absorptions close to the stellar radial velocities). Interstellar features in the Arcturus spectra would be found at −10 km s^{-1} from line center, while those of Aldebaran would be closer to −30 km s^{-1} (Redfield & Linsky 2002). A

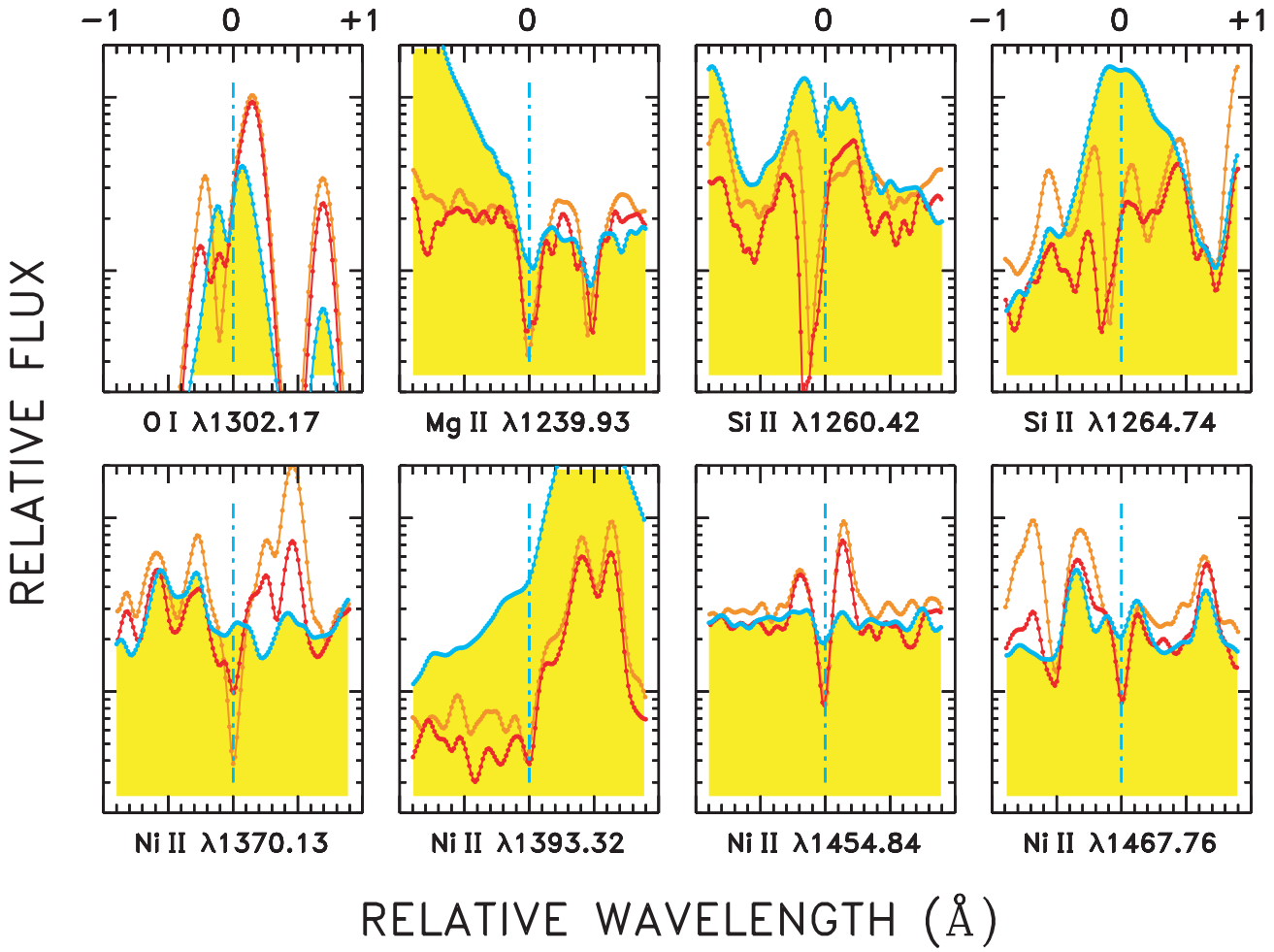

FIG. 4.—Selected ground-state absorption features from the far-UV interval. Abscissa scales are relative to the rest wavelengths of the transitions (indicated below each panel) in the stellar reference frame. Yellow shaded profiles (outlined by blue dotted curves) are from a composite active giant spectrum. Red and orange dotted curves refer to Arcturus and Aldebaran, respectively. The spectra illustrated in each frame were separately normalized to the integrated flux over the interval 1650–1660 Å, dominated by the chromospheric C I 1657 Å multiplet. The logarithmic flux scales were adjusted for each panel to highlight the salient features.

distinct sharp O I λ1302 ISM component is seen in Arcturus, but the corresponding feature in Aldebaran is obscured by wind absorption (the outflow coincidentally is at the same velocity as the Local Interstellar Cloud in that direction). The strong O I and Si II lines in the two red giants clearly show blueshifted wind absorption.

The Ni II lines are prominent and appear close to their rest wavelengths. These features are not interstellar, because they are not blueshifted by the (different) amounts expected for the two red giants, nor are they formed in the winds of either star, for the same reason. Instead, the Ni II absorptions probably arise in cooler layers of the low chromosphere. Ni II absorption of H_2 B0–X6 R0 indicates that the cold molecule-rich fluorescing layer is relatively deep seated, probably immediately beneath the chromosphere (as opposed to, say, in a circumstellar shell), while Ni II absorption of the blue wing of Si IV λ1393 indicates that the hot line also forms *below* the cool region where Ni II is able to scatter effectively.

Figure 4 also shows the absorption of the red wing of N V λ1238 by Mg II λ1239.925, and there is evidence of Fe II λ1550.274 absorption ($E_l \sim 2000$ cm^{-1}) in the blue wing of C IV λ1550 (see, e.g., Fig. 5, below), presumably from the same layer responsible for the Ni II features.

3.1.3. *Deblending* Si IV*, Continued*

Just as H_2 B0–X6 R0 appears to have fallen victim to optically thick absorption by Ni II, additional H_2 transitions might be similarly affected by other species, potentially confusing the simple branching-ratio approach. Thus, we employed a more empirical strategy, as illustrated in Figure 5.

The H_2 B0–X5 P3 blend in λ1402 is displaced about 30 km s^{-1} shortward of the Si IV line center, revealing at least the long-wavelength portion of the hot-line wing. Si IV λ1393, on the other hand, is strongly affected by the B0–X5 R0 and R1 transitions, particularly the former, which falls close to the Si IV line center. We modeled the combined Si IV+H_2 blends, using Gaussian profiles for the former and the intrinsic mean line shape for the latter described previously. We assumed that the reference Si IV profile applied to the λ1393 and λ1402 components with a 2:1 (effectively optically thin) line strength ratio. We also required that it be consistent with the C IV lines, again assuming a 2:1 ratio between the λ1548 and λ1550 components, because the Si IV and C IV features of normal coronal red giants (e.g., Pollux in Fig. 3) are nearly identical in shape.

Single-component Gaussian reference profiles yielded a poor match to the Si IV+C IV system. However, a two-component line shape—consisting of a main Gaussian of FWHM ∼ 130 km s^{-1} combined with a narrow peak of FWHM ∼ 50 km s^{-1} contributing ∼20% of the total flux, both centered at the stellar rest velocity—produced acceptable fits to the Si IV features of Arcturus and Aldebaran, as illustrated in Figure 5 (also for γ Dra, for which the H_2 blends are much weaker; see Fig. 3) and reproduced the C IV features, especially if one allows for additional emission blends in the λ1550 components. McMurry et al. (1999) described a Lyα–Fe II fluorescence process, evident in the earlier GHRS observations of Aldebaran, that produces the λ1550.501 emission excess in the blue wing of C IV λ1550 (near −50 km s^{-1}): the pumping line is Fe II λ1214.398, just shortward of Lyα line center. In our higher quality STIS profiles, a weaker fluorescent Fe II feature is present at λ1547.802 (−80 km s^{-1} from C IV λ1548 line center), pumped by Fe II λ1214.735, with a secondary component at λ1550.087 (−130 km s^{-1} from C IV λ1550). Another complex of Fe II lines, pumped by λ1216.769, appears at 1550.541, 1550.638, and 1551.107 Å. The first two produce the redward bump on Fe II λ1550.501, while the third component appears +60 km s^{-1} longward of C IV λ1550.

The core/halo character of the reference hot-line profiles deduced from the deblending strategy is reminiscent of the narrow/broad component line shapes of Si IV and C IV seen in normal coronal stars (e.g., Wood, Linsky, & Ayres 1997).

3.2. *Buried Coronae*

In short, there is evidence from optically thick absorptions by singly ionized species in Si IV λ1393, C IV λ1550, and N V λ1238 and C I recombination emission at N V λ1242 (with negligible N V emission, probably attenuated by C I line absorption in deeper layers) that the hot lines form *within* or *beneath* the extended chromospheric envelope in a layer capable of scattering radiation but of low thermal emissivity: a "cool absorber," if you will. Furthermore, Ni II absorption of H_2 λ1454 indicates that the cold fluorescing molecular layer lies beneath the cool absorber. Lack of strong CO A–X attenuation of the Si IV and C IV line shapes indicates formation *above* the cold molecular layer, and lack of Si I and C I continuum absorption (for $\lambda < 1520$ and 1240 Å, respectively) suggests that these latter species are mostly ionized in the cool absorber (probably by Lyα photoionization). Taken together, the evidence suggests that the structures responsible for the hot-line emission are at least partially submerged in the red giant chromosphere but extend beyond the cold molecular layer just above the stellar photosphere.

It seems then that the red giant coronae, metaphorically speaking, are *buried alive*. Ironically, the situation is qualitatively similar to the "smothered coronae" of classical T Tauri stars (Walter & Kuhi 1981), at the youngest stages of magnetic evolution.

Incidentally, the cold fluorescing layer in the red giant atmospheres might be related to an equally curious situation in the solar outer atmosphere: intrusions of cool gas between the top of the photosphere and the midchromospheric "canopy" level. The "COmosphere," as it has come to be called, is distinguished by $T \sim 3500$ K off-limb emissions in the 5 μm $\Delta v = 1$ rovibrational bands of CO; temperatures are about 1000 K cooler than the $T_{\min}$ of the Vernazza, Avrett, & Loeser (1976, hereafter VAL) semiempirical atmospheric models (see, e.g., Ayres 2002 and references to previous work therein).

3.3. *Atmospheric Extension: Importance of the Pressure Scale Height*

In the red giants, apparently, the structures that give rise to the hot-line emissions mostly do not manage to penetrate far enough into the outer atmosphere to escape X-ray attenuation by the thick chromosphere. The proposed scenario is depicted in Figure 6. The cartoon is based on an illustrative atmospheric stratification for Aldebaran taken from the recent one-dimensional semiempirical chromospheric model of McMurry (1999) and for the Sun from the VAL models (and Ayres & Rabin 1996 for the COmospheric component). Note that the atmospheres are

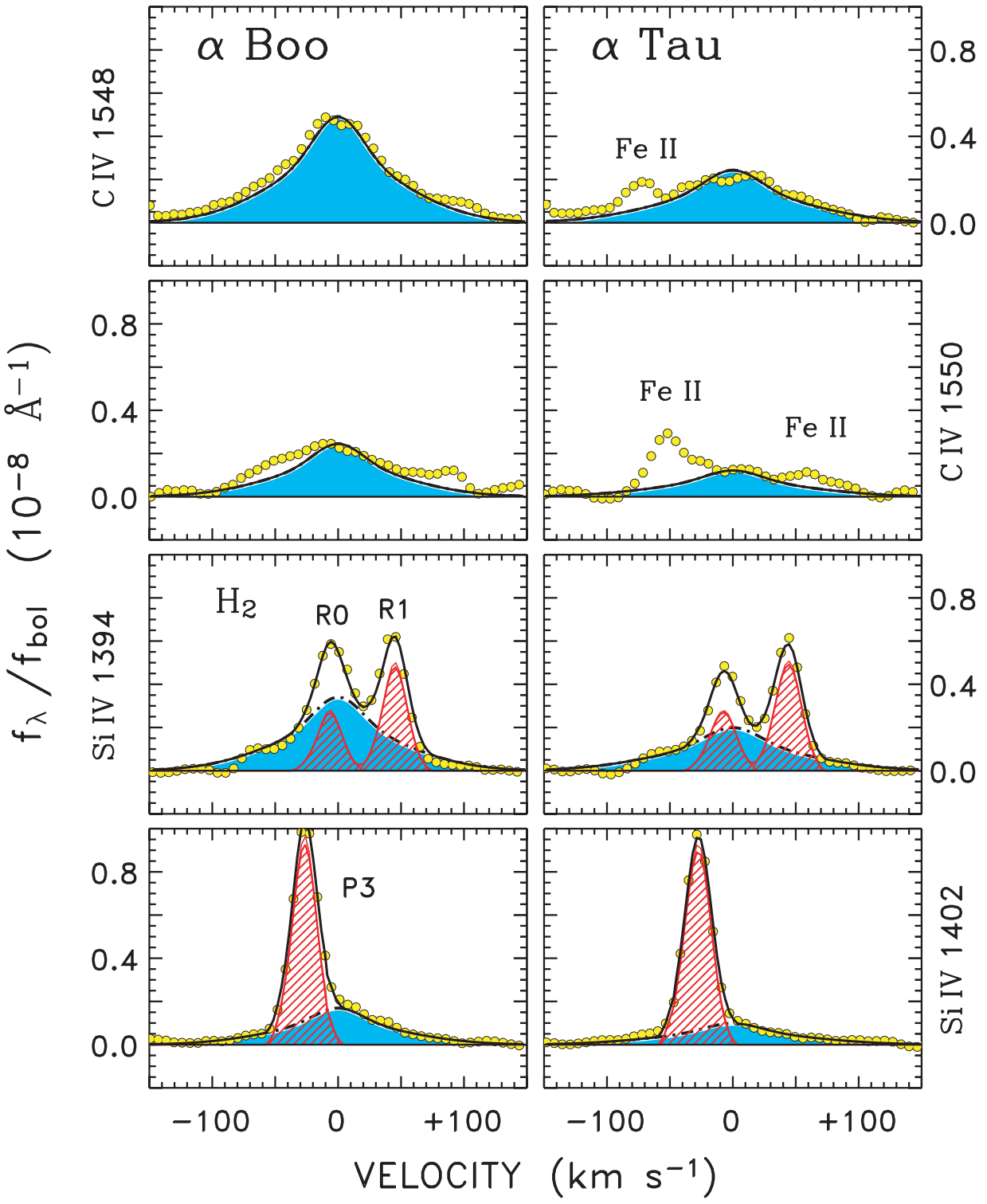

FIG. 5.—Details of deblending corrections and profile modeling for the Si IV (and C IV) lines. The ordinate scale is the observed flux density normalized by the bolometric flux, allowing a fairer comparison of the relative emission line strengths. In each panel, the shaded areas (outlined by black dot-dashed curves) are multiple-Gaussian profiles of the hot lines, while the red hatched line shapes in the Si IV panels are the best-fit H_2 B0–X5 blends. Yellow dots are the observed STIS line profiles, and the black solid curves are the total fits (i.e., Si IV plus H_2 in the Si IV panels). Note also the Fe II fluorescent blends present in both components of the C IV doublet (particularly evident in Aldebaran).

compared on an r/R_* scale: in physical units (e.g., r in centimeters), the red giant would be an additional factor of *40* times more extended. The enormous bloating arises because the atmospheric thickness is established mainly by the pressure scale height, $H_p \equiv kT/\mu g$, where μ is the mean molecular weight and the surface gravity g scales as M_*/R_*^2. The chromospheric temperatures of a red giant are similar to the Sun's, and the stellar mass also is close to solar. The red giant radius, however, is $R_* \sim 40$ in solar units. With $H_p/R_* \sim R_*$, even on a relative r/R_* scale the

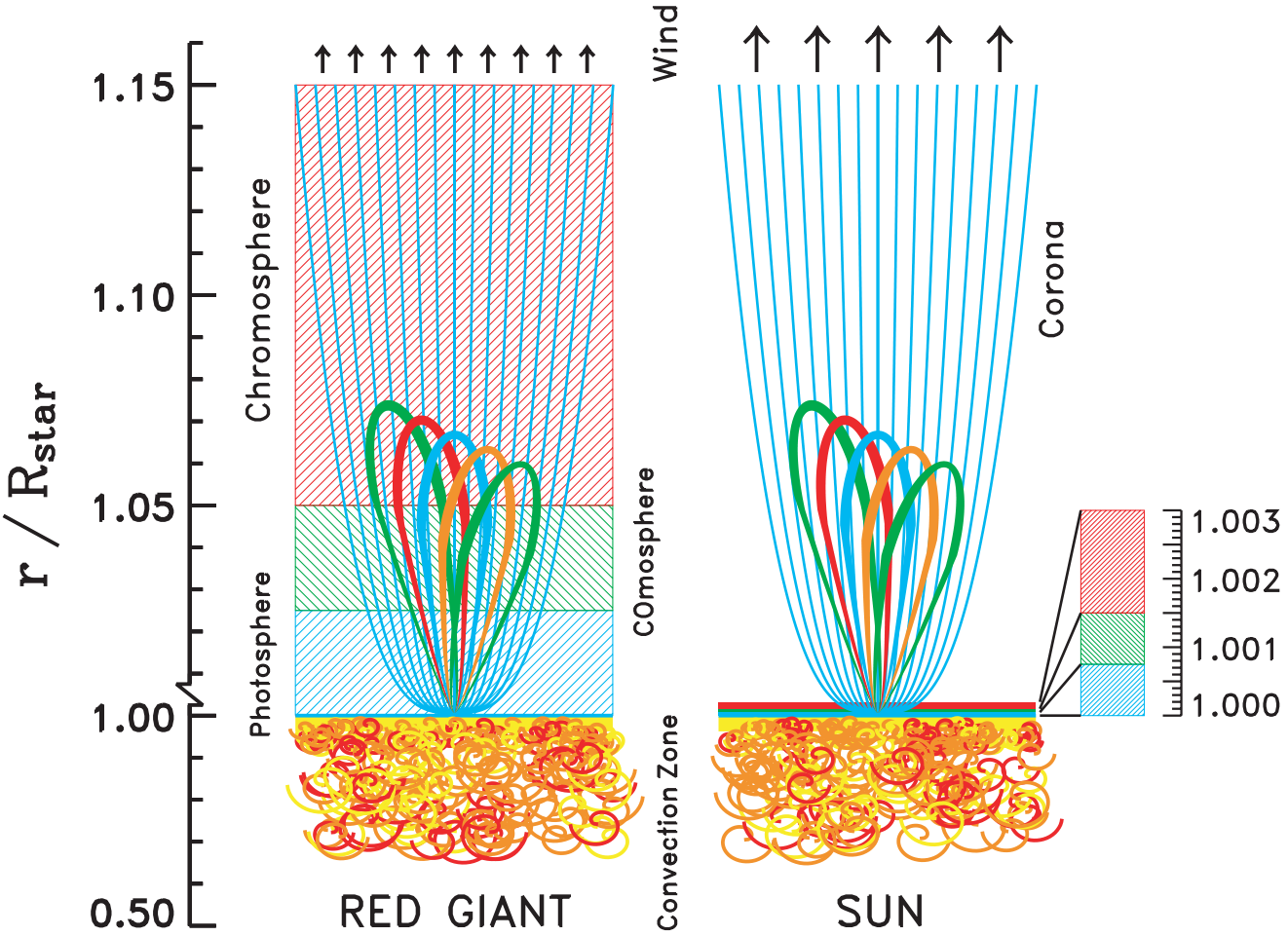

FIG. 6.—Cartoon of the buried corona scenario. A red giant atmosphere (patterned after semiempirical models of Aldebaran; *left*) and the Sun (*right*) are compared on an r/R_* scale (the enormous extension of the low-gravity giant atmosphere would be even more exaggerated on a physical r scale). The closed magnetic loop structures, depicted as similar in $\Delta r/R_*$ for the two stars, are assumed to have arisen from direct convective processes, thereby acquiring a scale length equal to some fraction of the depth of the surface convection zone (here $\Delta r_{\rm loop} \sim 25\%\ \Delta r_{\rm CZ}$). Coronal magnetic structures of that size would rise high above the compact solar atmosphere and radiate X-rays freely to space but be trapped within the extended X-ray–absorbing chromospheric envelope of the red giant.

red giant outer atmosphere will be enormously extended. This also is a minimal estimate: if *dynamical* pressure support is important, the effective scale height will be even larger than in the purely thermal case.

Anticipating the discussion section below, we propose that small-scale magnetic structures (as distinguished from dynamo-generated large-scale active regions) on the red giants, capable of supporting modest coronal activity, are produced in the near-surface layers of the upper convection zone (CZ) and have a scale length that is some fraction of the CZ thickness, say, 25% $\Delta r_{\rm CZ}$. The cartoon depicts the CZ depth of the Sun ($\Delta r_{\rm CZ} \sim 0.3\ R_\odot$) and that of a red giant (inferred from the two-dimensional simulations of Asida 2000), illustrating that they are similar fractions of the respective stellar radii. (Even if the red giant CZ is much deeper than indicated by the two-dimensional simulations, the contrast with the Sun still will be much smaller than H_p/R_*, simply because the solar CZ depth already is a large fraction of 1 $R_\odot$.) This in turn suggests that the nondynamo magnetic loops will be similar in scale for dwarfs and giants in terms of $\Delta r/R_*$. Such loops will rise high above the compact solar atmosphere, but their cousins will be trapped *within* the extended red giant chromosphere.

3.4. *X-Ray–Absorbing Columns*

We can estimate the X-ray–absorbing columns in the red giant chromosphere by appealing to semiempirical models developed to explain the Ca II H and K emission cores in Arcturus (e.g., Ayres & Linsky 1975) and more recent efforts to match a wider variety of UV lines in Aldebaran (McMurry 1999). These one-dimensional average models indicate a chromospheric column mass density ("overburden") of $m \sim 0.3$ g cm^{-2}, corresponding to a hydrogen column density of $N_{\rm H} \sim 1 \times 10^{23}$ cm^{-2} for a helium abundance of 10% (by number). The optically thick Ni II absorptions provide a second constraint. Using log gf values from the Kurucz line list (Kurucz & Bell 1995), an Ni abundance for mildly metal-depleted Arcturus of 5×10^{-7} with respect to hydrogen (Peterson, Dalle Ore, & Kurucz 1993), and a line Doppler width of 5 km s^{-1}, we obtain $N_{\rm H} \sim 2 \times 10^{20} \tau_{\rm Ni\ II}$, assuming that all the nickel is singly ionized. We do not know $\tau_{\rm Ni\ II}$, however, except that it likely is $\gg 1$.

WebPIMMS simulations for *ROSAT* PSPC and *Chandra* HRC-I, using solar-abundance Raymond-Smith models at several temperatures between log $T = 5.8$ and 6.8, show that tenfold 0.2–2 keV X-ray absorption sets in at

$N_H \sim 5 \times 10^{20}$ cm^{-2} on the cooler side of the temperature range and at $N_H \sim 5 \times 10^{21}$ cm^{-2} on the hotter side. The N_H estimated from the chromospheric models exceeds these critical-attenuation values, while that from the Ni II absorption constraint will be comparable if $\tau_{Ni\ II} \gtrsim 10$.

Plausibly, then, the thick chromospheres of the red giants can provide an effective opacity barrier to prevent the escape of coronal X-rays that might be produced in the lower atmosphere. (Note, however, that Haisch, Schmitt, & Fabian 1992 demonstrated that the extended *winds* of the red giants would lack sufficient column densities to significantly attenuate any X-rays emitted from the *top* of the chromosphere.) The likely situation is that most of the coronal loops are entirely buried in the red giant chromosphere and their X-rays severely degraded, while a few of the (longer) loops might penetrate into the X-ray–thin regime and thereby be detectable at kilovolt energies.

4. DISCUSSION

Although the "coronal" structures of the red giants are only tentatively observed in X-rays, their existence is clearly indicated indirectly by the hot-line emissions recorded by *HST* and *FUSE*. The submerged coronal zones are too hot and their emission line widths are too supersonic to be attributed to ordinary acoustic shock heating: the maximum temperature excursions in the low chromosphere are less than 10^4 K in the one-dimensional hydrodynamical wave-heating simulations of giant stars by Cuntz, Rammacher, & Ulmschneider (1994). Instead, the hot zones likely are powered by a magnetic process, perhaps related to the small-scale UV-bright points of the solar supergranulation network. At the same time, the very large chromospheric radiative losses (primarily in atomic hydrogen and oxygen) compared with the small subcoronal emissions (e.g., in C IV and O VI) suggest that the hot magnetic structures are a relatively minor contributor to the overall energy balance of the chromosphere (unless the hot-line emissions represent only a small fraction of the overall heating dissipated in the magnetic structures).

4.1. *Dynamoless Fields?*

Of course, assigning the hot-line structures to a magnetic source begs the fundamental question that fueled the original discussions of the noncoronal giants, namely, how can any magnetic dynamo action survive on ancient spun-down stars? Strong dynamo action is thought to require the shearing action of velocity fields in a thin zone—the tachocline (Spiegel & Zahn 1992)—separating the bottom of the differentially rotating convection zone from the rigidly rotating radiative interior (e.g., Gilman 2000). The dynamo is held responsible for the decade-long cyclic ebb and flow of sunspots, the most conspicuous signature of solar activity. Nevertheless, at the minimum of the activity cycle when there often are long intervals with few or no sunspots on the disk, the solar corona does not simply vanish but in fact maintains a soft X-ray emission level that might be only a factor of 5 less than at cycle maximum when the disk is heavily spotted (Judge et al. 2003). EUV filtergrams taken in Fe XII λ195 (2×10^6 K) by the Extreme-Ultraviolet Imaging Telescope (EIT) of the *Solar and Heliospheric Observatory* (*SOHO*) and by the *Transition Region and Coronal Explorer* (*TRACE*) show a haze of relatively low-altitude ($h \lesssim 50,000$ km) coronal emission nearly ubiquitously covering the disk, over a uniformly distributed sprinkling of compact X-ray "bright points," seen throughout the cycle. The difference near cycle maximum is the increased presence of "active regions": sites of concentrated coronal emissions, often distinguished by extensive systems of bright loops rising high ($h \gtrsim 200,000$ km) above the solar surface.

The background corona in the relatively soft EIT and *TRACE* images appears to be persistent and nearly constant throughout the sunspot cycle and thus perhaps arises from a different magnetic source than the active regions spawned by the classical dynamo. Title & Schrijver (1998) concluded on the basis of *SOHO* Michelson Doppler Imager observations of the recycling of surface fields that the magnetic flux responsible for small-scale "ephemeral regions," which ultimately populates the global supergranulation pattern, must have a source relatively close to the solar surface. They invoked an "α^2" magnetic generation process, which relies purely on convective turbulence and thus applies equally well to nonrotating, noncycling stars.

Such a mechanism is an appealing explanation for the presence of hot-line emission on noncoronal red giants. If small-scale magnetic fields indeed are present in the lower atmospheres of Arcturus and Aldebaran, it is natural to ask whether they might in some way be responsible for initiating the cool outflows of such stars. The wind-driving mechanism in red giants has long been elusive, and viable candidates are in short supply (e.g., Sutmann & Cuntz 1995). At the same time, such winds arguably are important in recycling nuclear-processed material in the galaxy, particularly given the large population of $\sim 1\ M_\odot$ stars that become red giants, compared with the extremely rare massive stars that ultimately disperse their chemically enriched envelopes in supernova events. While a full discussion of the wind-driving issue is beyond the scope of this paper, we note that Rosner et al. (1995) argued that the magnetic loop topology on inactive red giants should favor open-field structures, such as those in which the acceleration of the solar wind is thought to occur (Withbroe, Feldman, & Ahluwalia 1991).

4.2. *Opacity Holes*

There are serious shortcomings in traditional one-dimensional model stratifications of red giant atmospheres for explaining the observed rich fluorescence spectra of CO and H_2, simply because it is very difficult to irradiate the lower cooler layers of the atmosphere, where the molecules in principle reside, all the way from the upper hotter layers, where the pumping emissions (O I and H I, respectively) are thought to form (Ayres 1986; McMurry & Jordan 2000). In particular, the large optical depths of the chromosphere in these strong resonance lines will thermalize the radiation fields, thus producing a homogenization in frequency that yields a very different and much weaker molecular fluorescent pattern than observed. Furthermore, the large columns of atomic carbon and silicon in the chromosphere also will degrade downward, propagating Lyα and O I triplet (1305 Å) photons by photoionization, and the Si I continuum opacity likewise will attenuate any *outward* escaping fluorescent radiation, at least shortward of the edge at 1520 Å. Nevertheless, there is no obvious break in, say, the CO fluorescent properties at that wavelength. These considerations point to a scenario in which the pumping radiation is

produced in relatively close proximity to the cold molecular gas, where the fluorescent excitation is mainly horizontal rather than vertical (e.g., Ayres 1986).

An inhomogeneous scenario for the fluorescence is important, because it might tie closely into the buried corona hypothesis. In particular, the compact magnetic flux tubes of the solar supergranulation pattern produce strongly elevated low-altitude chromospheric radiation (as well as hotter lines such as C IV; see Reeves et al. 1974). If the buried fields of the red giants are similar, they could act as strong local radiation sources along the full vertical extent of the structures. Lyα photons penetrating horizontally into the surrounding gas would photoionize both Si and C out to characteristic Strömgren radii but could not photodissociate (or photoionize) CO or H_2. Within the cylindrical ionization zone, Lyα and O I photons would be able to excite transitions of H_2 and CO, respectively, and the fluorescent emissions could escape vertically through the photoionized opacity hole.

If the horizontal extent of the ionization zone is much larger than the vertical thickness of the molecular COmosphere, one can understand why CO fluorescence simulations indicate a large molecular column density to produce the observed fluorescence, but at the same time the red giant far-UV spectrum does not generally display evidence for discrete strong CO absorption features: the stratified atmosphere *outside* the opacity holes would produce its continuum emission spectrum from hotter layers *above* the molecular zone, and only in the opacity holes themselves would one be able to see down into the COmosphere in the ultraviolet and thus record any potential absorption (or emission) signatures. Since the hot magnetic tubes with their associated opacity holes likely are a sparsely distributed minority component on the surface, only species unique to them, such as the fluorescent emissions or the hot lines, would be able to display noticeable molecular absorption effects in the spatially average spectrum.

5. CONCLUSIONS

The tentative detection of X-rays from Arcturus indicates that the hot-line emission zones might be capable of attaining truly coronal temperatures ($T \sim 10^6$ K). This, with the definite presence of material at a few times 10^5 K, points to a magnetic origin for the hot structures and is sufficient to eliminate the other potential heating candidate, namely, acoustic shocks. The observed high temperatures also greatly exceed the "cool loop" equilibrium value of a few times 10^4 K proposed by Antiochos et al. (1986), who sought to explain the Linsky-Haisch coronal dividing line in terms of a bifurcated coronal loop solution that collapses onto the cool branch when the stellar surface gravity drops below a critical level.

The important conclusion is that the old red giants still are able to sustain a modest level of magnetic activity complete with subcoronal structures perhaps analogous to the magnetic fragments of the solar supergranulation network (which radiate primarily in $T < 10^6$ K lines). The residual surface magnetism might play an unforeseen role in the acceleration of the red giant winds: the solar network is the site of *spicules,* transient jets of chromospheric-temperature material that carry a substantial amount of mass into the corona—10 times that lost in the solar wind—most of which must drain back to the surface (Beckers 1968). Solar spicules very likely are driven by magnetic reconnection, and perhaps there are analogous events on red giants that contribute to their own mass loss. Indeed, the large nonthermal line widths of the Si IV and C IV emissions of Arcturus and Aldebaran point to a strongly dynamic formation mechanism, perhaps related to the "explosive events" seen in the solar magnetic network dominantly at 10^5 K temperatures (Moses & Cook 1994).

6. FOR THE FUTURE

Given that Arcturus is tentatively detected as a weak coronal source, can we hope to learn more about its coronal properties by using one of the current generation of energy-resolving X-ray instruments? The best choice is the pn camera on *XMM-Newton*, which can be used with the thick filter option and a partial window readout mode to suppress the optical contamination from a $m_V \sim 0$ red giant.[5] Simulations with WebPIMMS for a range of coronal temperatures and absorption columns predict a total count rate of $\sim 1 \times 10^{-3}$ counts s^{-1} if the source is very soft ($T \sim 1 \times 10^6$ K), or about 100 counts in 10^5 s (for a 75% encircled energy radius of 20″ [$E \lesssim 1.5$ keV]; Fig. 6 in Ehle et al. 2003). The quiescent background in the detect circle for the same exposure would be comparable, however. This combination might be sufficient to determine a crude hardness ratio but not to spectrally distinguish unambiguously between an unabsorbed—but faint—source or a stronger one, heavily absorbed. Thus, while the long-standing mystery of whether Arcturus is an X-ray source seems finally to have been resolved, at least tentatively, the details of the physical nature of the red giant corona appear destined to remain buried for some time to come.

This work was supported by *Chandra* grant G02-3014X from the Smithsonian Astrophysical Observatory, *HST* grant GO-09273.01-A from the Space Telescope Science Institute, and NASA grant NAG 5-13058. Observations from the *Chandra X-Ray Observatory* were collected and processed at the *Chandra* X-Ray Observatory Center, operated for NASA by Smithsonian Astrophysical Observatory. Observations from the NASA/ESA *HST* were collected at the STScI, operated by AURA, under contract NAS 5-26555. *FUSE* is operated for NASA by Johns Hopkins University under contract NAS 5-32985. This research also utilized the SIMBAD database, maintained by CDS, Strasbourg, France, the *ROSAT* public archive, and the WebPIMMS count rate tool at HEASARC of the NASA Goddard Space Flight Center.

[5] See http://xmm.vilspa.esa.es/docs/documents/CAL-TN-0001-1-0.ps.

REFERENCES

Abgrall, H., Roueff, E., Launay, F., Roncin, J. Y., & Subtil, J. L. 1993, A&AS, 101, 273
Antiochos, S. K., Haisch, B. M., & Stern, R. A. 1986, ApJ, 307, L55
Asida, S. M. 2000, ApJ, 528, 896
Ayres, T. R. 1986, ApJ, 308, 246
———. 2000, Sol. Phys., 193, 273
———. 2002, ApJ, 575, 1104
Ayres, T. R., Fleming, T. A., & Schmitt, J. H. M. M. 1991, ApJ, 376, L45
Ayres, T. R., & Linsky, J. L. 1975, ApJ, 200, 660
Ayres, T. R., Linsky, J. L., Vaiana, G. S., Golub, L., & Rosner, R. 1981a, ApJ, 250, 293
Ayres, T. R., Moos, H. W., & Linsky, J. L. 1981b, ApJ, 248, L137
Ayres, T. R., & Rabin, D. 1996, ApJ, 460, 1042
Ayres, T. R., Simon, T., Stern, R. A., Drake, S. A., Wood, B. E., & Brown, A. 1998, ApJ, 496, 428
Ayres, T. R., et al. 1995, ApJS, 96, 223
———. 1997, ApJ, 491, 876
———. 2003, ApJ, 583, 963
Beckers, J. M. 1968, Sol. Phys., 3, 258
Brown, A., Linsky, J. L., & Ayres, T. R. 1993, in AIP Conf. Proc. 313, The Soft X-Ray Cosmos, ed. E. M. Schlegel & R. Petre (New York: AIP), 36
Cuntz, M., Rammacher, W., & Ulmschneider, P. 1994, ApJ, 432, 690
Ehle, M., et al., eds. 2003, *XMM-Newton* Users' Handbook, Version 2.1 (Vilspa: *XMM-Newton* Science Operations Center)
Gehrels, N. 1986, ApJ, 303, 336
Gilman, P. A. 2000, Sol. Phys., 192, 27
Gray, D. F., & Pallavicini, R. 1989, PASP, 101, 695
Haisch, B., Schmitt, J. H. M. M., & Fabian, A. C. 1992, Nature, 360, 239
Hasinger, G., Burg, R., Giacconi, R., Schmidt, M., Trumper, J., & Zamorani, G. 1998, A&A, 329, 482
Holzwarth, V., & Schüssler, M. 2001, A&A, 377, 251
Judge, P. G., Solomon, S. C., & Ayres, T. R. 2003, ApJ, 593, 534
Kraft, R. P., Burrows, D. N., & Nousek, J. A. 1991, ApJ, 374, 344
Kurucz, R. L., & Bell, B. 1995, CD-ROM 23, Atomic Line Data (Cambridge: SAO)
Lindler, D. 1999, STIS-IDT CALSTIS Manual, Version 1999 April (Greenbelt: NASA/LASP)
Linsky, J. L., & Haisch, B. M. 1979, ApJ, 229, L27
McMurry, A. D. 1999, MNRAS, 302, 37
McMurry, A. D., & Jordan, C. 2000, MNRAS, 313, 423
McMurry, A. D., Jordan, C., & Carpenter, K. G. 1999, MNRAS, 302, 48
Micela, G., et al. 1988, ApJ, 325, 798
Moos, W. H., et al. 2000, ApJ, 538, L1
Moses, D., & Cook, J. W. 1994, Space Sci. Rev., 70, 81
Murray, S. S., et al. 1997, Proc. SPIE, 3114, 11
Neuhauser, R., & Comeron, F. 1998, Science, 282, 83
Parker, E. N. 1970, ARA&A, 8, 1
Peterson, R. C., Dalle Ore, C. M., & Kurucz, R. L. 1993, ApJ, 404, 333
Redfield, S., & Linsky, J. L. 2002, ApJS, 139, 439
Reeves, E. M., et al. 1974, ApJ, 188, L27
Robinson, R. D., Carpenter, & K. G., Brown, A. 1998, ApJ, 503, 396
Rosner, R., Musielak, Z. E., Cattaneo, F., Moore, R. L., & Suess, S. T. 1995, ApJ, 442, L25
Rutledge, R. E., Basri, G., Martín, E. L., & Bildsten, L. 2000, ApJ, 538, L141
Sahnow, D. J., et al. 2000, ApJ, 538, L7
Schmitt, J. H. M. M. 1997, A&A, 318, 215
Simon, T., & Drake, S. A. 1989, ApJ, 346, 303
Spiegel, E. A., & Zahn, J.-P. 1992, A&A, 265, 106
Sutmann, G., & Cuntz, M. 1995, ApJ, 442, L61
Title, A. M., & Schrijver, C. J. 1998, in ASP Conf. Ser. 154, Tenth Cambridge Workshop on Cool Stars, Stellar Systems and the Sun, ed. R. A. Donahue & J. A. Bookbinder (San Francisco: ASP), 345
Tuominen, I., Moss, D., & Rüdiger, G., eds. 1991, IAU Colloq. 130, The Sun and Cool Stars: Activity, Magnetism, Dynamos (New York: Springer)
Vernazza, J. E., Avrett, E. H., & Loeser, R. 1976, ApJS, 30, 1 (VAL)
Walter, F. M., & Kuhi, L. V. 1981, ApJ, 250, 254
Watson, M. G., et al. 2001, A&A, 365, L51
Weisskopf, M. C., O'Dell, S. L., & van Speybroeck, L. P. 1996, Proc. SPIE, 2805, 2
Withbroe, G. L., Feldman, W. C., & Ahluwalia, H. S. 1991, in Solar Interior and Atmosphere, ed. A. N. Cox, W. C. Livingston, & M. S. Matthews (Tucson: Univ. Arizona Press), 1087
Wood, B. E., Linsky, J. L., & Ayres, T. R. 1997, ApJ, 478, 745
Woodgate, B. E., et al. 1998, PASP, 110, 1183